Pure and Applied Geophysics

CrossMark

Numerical Simulation of M9 Megathrust Earthquakes in the Cascadia Subduction Zone

D. Roten,[1] K. B. Olsen,[1] and R. Takedatsu[1]

Abstract—We estimate ground motions in the Pacific North-west urban areas during M9 subduction scenario earthquakes on the Cascadia megathrust by simulating wave propagation from an ensemble of kinematic source descriptions. Velocities and densities in our computational mesh are defined by integrating the regional Cascadia Community Velocity Model (CVM) v1.6 (Stephenson et al. P-and S-wave velocity models incorporating the Cascadia subduction zone for 3D earthquake ground motion simulations— update for open-file report 2007–1348, US Geological Survey, 2017) including the ocean water layer with a local velocity model of the Georgia basin (Molnar, Predicting earthquake ground shaking due to 1D soil layering and 3D basin structure in SW British Columbia, Canada, 2011), including additional near-surface velocity information. We generate six source realizations, each consisting of a background slip distribution with correlation lengths, rise times and rupture velocities consistent with data from previous megathrust earthquakes (e.g., 2011 M 9 Tohoku or 2010 M 8.8 Maule). We then superimpose $M \sim 8$ subevents, characterized by short rise times and high stress drops on the background slip model to mimic high-frequency strong ground motion generation areas in the deeper portion of the rupture (Frankel, Bull Seismol Soc Am 107(1):372–386, 2017). The wave propagation is simulated using the discontinuous mesh (DM) version of the AWP finite difference code. We simulate frequencies up to 1.25 Hz, using a spatial discretization of 100 m in the fine grid, resulting in surface grid dimensions of $6540 \times 10{,}728$ mesh points. At depths below 8 km, the grid step increases to 300 m. We obtain stable and accurate results for the DM method throughout the simulation time of 7.5 min as verified against a solution obtained with a uniform 100 m grid spacing. Peak ground velocities (PGVs) range between 0.57 and 1.0 m/s in downtown Seattle and between 0.25 and 0.54 m/s in downtown Vancouver, while spectral accelerations at 2 s range between 1.7 and 3.6 m/s^2 and 1.0 and 1.3 m/s^2, respectively. These long-period ground motions are not significantly reduced if plastic Drucker-Prager yielding in shallow cohesionless sediments is taken into account. Effects of rupture directivity are significant at periods of ~ 10 s, but almost absent at shorter periods. We find that increasing the depth extent of the subducting slab from the truncation at 60 km in the Cascadia CVM version 1.6 to ~ 100 km increases the PGVs by 15% in Seattle and by 40% in Vancouver.

Key words: Long-period ground motion, wave propagation simulation, megathrust earthquake, finite difference method.

[1] San Diego State University, San Diego, CA, USA. E-mail: droten@sdsu.edu

Birkhäuser

1. Introduction

The Cascadia subduction zone, which extends from the Mendocino Triple Junction northwards to Vancouver Island, marks the ~ 1000 km long boundary between the Juan de Fuca (JdF) plate to the west and the North American (NA) plate to the east (Fig. 1). The paleoseismic record shows that the Cascadia subduction zone has repeatedly produced large megathrust earthquakes ($M > 8$) with a recurrence period of approximately 500 years (Heaton and Hartzell 1986; Witter et al. 2012; Goldfinger et al. 2017). The last M9 Cascadia earthquake, which occurred in 1700 A.D. is well documented from native stories, Japanese records and radiocarbon tree-ring dating (Ludwin et al. 2005). A Cascadia megathrust earthquake represents a major source of seismic hazard to the Pacific Northwest, in particular to the large metropolitan areas of Seattle (population 3.8 M), Vancouver (population 2.5 M) and Portland (population 2.4 M), which are located on top of deep sedimentary basins that could further amplify the seismic waves (Cassidy and Rogers 2004; Frankel et al. 2009).

Because no Cascadia megathrust earthquake has occurred since the onset of instrumental seismology, numerical simulations of wave propagation represent our best option to estimate the level of ground motion to be expected during the next such event. The first 3D simulations of a M9 Cascadia megathrust earthquake by Olsen et al. (2008) used a long-period ($f < 0.5$ Hz) source model obtained by mapping slip inversion results of the M_w 9.1–9.3 Sumatra–Andaman earthquake (Han et al. 2006) onto the Cascadia subduction slab. The simulations of Olsen et al. (2008) were done using the first version of the community velocity model (CVM) for the Pacific
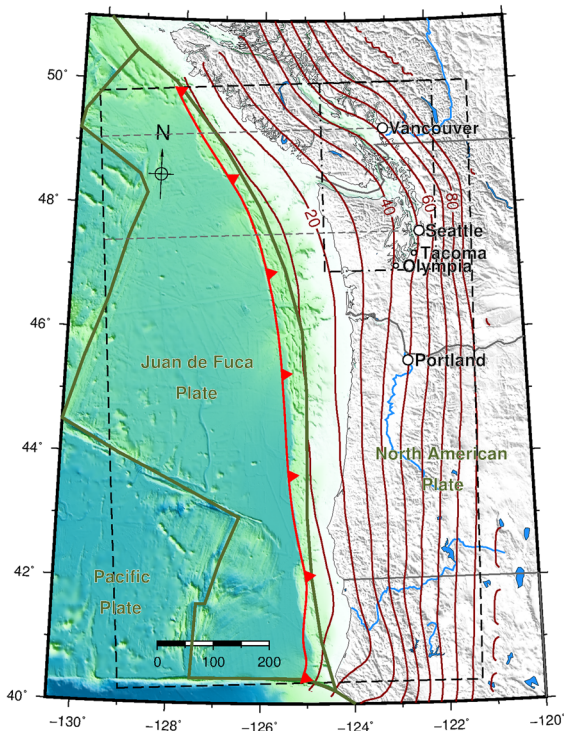
Figure 1
Plate boundaries (dark green lines) in the Cascadia area and oceanic trench (thick solid red line). The dashed rectangle outlines the extent of the computational domain; the dash-dotted inner rectangle shows the extent of the Georgia basin CVM. Red contours show the depth of the subduction slab [in km, from (Blair et al. 2011; McCrory et al. 2012)]. Dashed gray (E–W) lines depict profiles along which cross-sections are shown in Fig. 2

Northwest (Stephenson 2007), which incorporates continental and oceanic sedimentary basin, crust and mantle units. The 3D simulations predicted peak ground velocities of up to 0.42 m/s and shaking durations of up to 5 min in the Seattle area, which would represent a significant threat to high-rise buildings (Olsen et al. 2008).

More recently, Molnar (2011) and Molnar et al. (2014) developed a refined version of the CVM for the Georgia basin region by including shallow (< 1 km) high-resolution velocity information from geologic maps, P-wave tomography, boreholes and seismic surveys. Molnar et al. (2014) simulated a total of 10 deep JdF plate earthquakes, including the 2001 M 6.8 Nisqually earthquake, and found that the updated velocity model reproduces PGVs observed in the Vancouver area more accurately than the base Pacific Northwest CVM.

Both previous simulations efforts (Olsen et al. 2008; Molnar et al. 2014) used a spatial discretization of 250 m and a minimum shear-wave velocity of 625 m/s, restricting the frequency content of synthetic ground motions that can be accurately predicted to less or equal 0.5 Hz. This limitation reduces the usability of deterministic simulations for the purpose of predicting building response, as the frequency band of engineering interest extends to at least 10 Hz. Here, we present higher-resolution ($\Delta h = 100$ m) simulation results for M9 Cascadia megathrust earthquakes, where deterministic ground motions are predicted for a maximum frequency of 1.25 Hz.

More recently, Frankel et al. (2018) and Wirth et al. (2018) generated broadband synthetic seismograms for large megathrust earthquakes in the framework of the M9 project. Their synthetic seismograms were created using a hybrid procedure, which combined low-frequency ($f < 1$ Hz) 3D finite difference simulations with high-frequency ($f > 1$ Hz) stochastic signals. The M9 project revealed strong directivity effects and amplification in the Seattle basin at periods above 1 s.

2. Computational Model Domain

The computational domain includes the entire region covered by the Cascadia CVM and stretches from 40.2 to 50°N latitude and from 129 to 122°W longitude (Fig. 1). P-wave velocities, S-wave velocities and densities were adopted from version 1.6 of the CVM (Stephenson et al. 2017). P-wave velocities in the Cascadia CVM are based on available data for the continental crust and mantle and for the oceanic units, with S-wave velocities and densities derived from P-wave velocities using an empirical relationship (Brocher 2005). Inside continental sediments, both P- and S-wave velocities are derived from geological and geophysical information about the Quaternary and Tertiary deposits, including borehole data, seismic surveys and V_{S30} measurements. The Cascadia subduction interface is modeled after data from earthquake locations and seismic velocity studies (Blair et al. 2011; McCrory et al. 2012). We obtained the Cascadia CVM in 500 m resolution and
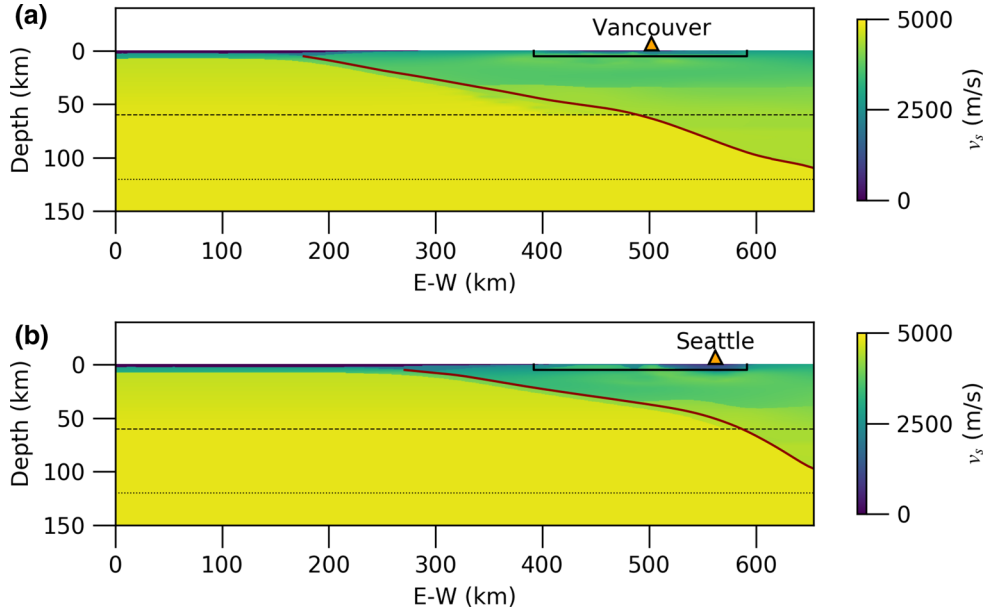
Figure 2
Vertical cross-sections (see locations in Fig. 1) of shear-wave velocity v_s along profiles from west to east through **a** Vancouver and **b** Seattle (triangles). The solid dark red line shows the upper slab surface (Blair et al. 2011; McCrory et al. 2012). Horizontal dashed and dotted lines show the vertical extent of the 60 and 120 km deep models, respectively. The black solid line marks the extent of the Georgia basin CVM (Molnar et al. 2014)

resampled it to 100 m resolution using linear interpolation.

Inside the Georgia basin and Puget Sound regions (dash-dotted rectangle in Fig. 1), we adopted material properties from the refined version of the Cascadia CVM (Molnar et al. 2014) (thereafter referred to as Georgia basin CVM), which is available in 250 m resolution. The Georgia basin CVM includes a more accurate description of the velocity structure in southwest British Columbia (Molnar et al. 2014), which is derived from local geological and geophysical datasets and the higher-resolution local tomography model of Dash et al. (2007). In order to avoid sharp contrasts at the intersection between the Cascadia CVM version 1.6 and the Georgia basin CVM, we defined a 20 km wide transition zone in which material properties of the two CVMs are gradually weighted using a ramp taper. At depths below 5 km, the Cascadia CVM version 1.6 was always used. Figure 2 shows shear-wave velocities along two profiles through Vancouver and Seattle, respectively.

Along the vertical direction, the Cascadia CVM includes the region between mean sea level (0 km) and 60 km depth (Stephenson et al. 2017), which is relatively shallow with respect to the horizontal extent. However, the top of the subducted slab is deeper than 60 km in the NE corner of the domain (Fig. 1). To investigate the effect of the deeper slab geometry on ground motions in the Vancouver and Seattle areas, we extended the Cascadia CVM to 120 km depth. We used the 3-D geometry of the subducted JdF plate for the region (Blair et al. 2011) and assigned the Cascadia CVM properties for oceanic mantle to volumes below the slab and deeper than 60 km (Fig. 2). Inside regions located above the slab but below 60 km depth, shear-wave velocities were extracted from a 3-D tomography model of the western United States (Chai et al. 2015), which also provides P-wave velocities and densities based on empirical relationships. We included the ocean water layer defined by v_p = 1500 m/s, v_s = 0, and density ρ = 1025 kg/m^3, incorporated above the sea bottom interface defined within the Cascadia CVM. Realistic

bathymetry was included because no numerical difficulties were encountered along the solid–liquid interface. However, land topography was not included, as support for irregular surface topography in AWP is currently still under development.

3. Kinematic Source Realizations

Near-source strong motion observations made during the 2010 M_w 8.8 Maule, Chile and the 2011 M_w 9–9.1 Tohoku earthquake have significantly improved our understanding of the rupture process pertaining to great ($M > 8.5$) subduction zone interface earthquakes. The rupture process of both earthquakes exhibited variations in the predominant frequency of radiation as a function of depth. In particular, low-frequency (~ 0.2 Hz) energy was radiated from shallow regions close to the trench, and short-period (~ 1 Hz) energy was emitted from deeper areas of the subducting slab (e.g., Wang and Mori 2011a; Lay et al. 2012).

In the case of the Tohoku earthquake, two major slip events with long rise time (~ 40 s) occurred at shallow depths close to the trench (e.g., Frankel 2013). This background slip, which produced up to 60 m of displacement that triggered the destructive tsunami (Hayashi et al. 2011), was well resolved from inversion of local and teleseismic records (e.g., Suzuki et al. 2011) and long-period back-projections (e.g., Roten et al. 2012). On the other hand, back-projections of short-period teleseismic P-waves located the source below the Honshu coastline (e.g., Koper et al. 2011; Wang and Mori 2011b). Long-period inversions of teleseismic arrivals from the Maule earthquake identify most of the slip to the north and south (up-dip) of the hypocenter (e.g., Delouis et al. 2010), while back-projections of P-waves trace the origin of high-frequency energy to roughly the same depth as the hypocenter (~ 35 km).

Because the short-period ($f > 0.1$ Hz) waves emitted from the deeper part are mainly relevant for engineering, efforts to predict ground motions from large megathrust earthquakes must take the frequency-dependence nature of such events into account. Frankel (2017) modeled the 2010 Maule

Figure 3 ▶

Surface projection of the megathrust rupture. **a** Fault surface with 25 km contours of along-strike and along-dip distances. **b** M 9.1 background slip and **c** M 7.9–8.1 subevents in rupture model D, including extent of locked (orange) and transition (light green) zones (Hyndman and Wang 1995) on the subducting slab (in 10 km contours) **d** Compound slip in rupture model Ds, with solid gray contours showing rupture times in 5 s intervals

earthquake using a kinematic rupture model, which consisted of a background slip distribution with long rise times and superimposed high stress-drop asperities with short rise times, and obtained a good match between simulated and observed spectral accelerations.

Kurahashi and Irikura (2011, 2013) created a short-period source model of the 2011 Tohoku earthquake which consisted of five subevents identified as strong motion generation areas, and generated synthetic ground motions using the empirical Green's function method. Galvez et al. (2016) introduced a dynamic rupture model of the Tohoku earthquake which involved rupture reactivation on the main near-trench slip area connected to a second large slip area by deeper, small asperities with high stress drop.

For the M9 Cascadia simulations presented here, we created a suite of compound kinematic source models using a similar method as Frankel (2017). The background slip distribution was generated using a von Karman autocorrelation function. Because empirical relationships for stochastic characterizations of earthquake slip are only available for crustal earthquakes (Mai and Beroza 2002), autocorrelation distances (100 km $\leq a_{x,z} \leq 1000$ km) and the Hurst coefficient ($H = 0.75$) were manually chosen to obtain a rough visual agreement with slip inversion results (Frankel 2017; Wirth et al. 2017). This approach results in a heterogeneous slip distribution with several large asperities, with correlation lengths consistent with rupture models of the 1700 Cascadia earthquake inferred from microfossil-based subsidence estimates (Wang et al. 2013). At the edges of the rupture surface, slip was gradually tapered to zero within a 200–300 km wide area bound by two concentric ellipses to avoid a box-like appearance of the final slip distribution.

In order to map the planar slip distribution onto the irregular fault geometry (Roten et al. 2011), we created a grid of along-strike and along-dip distances
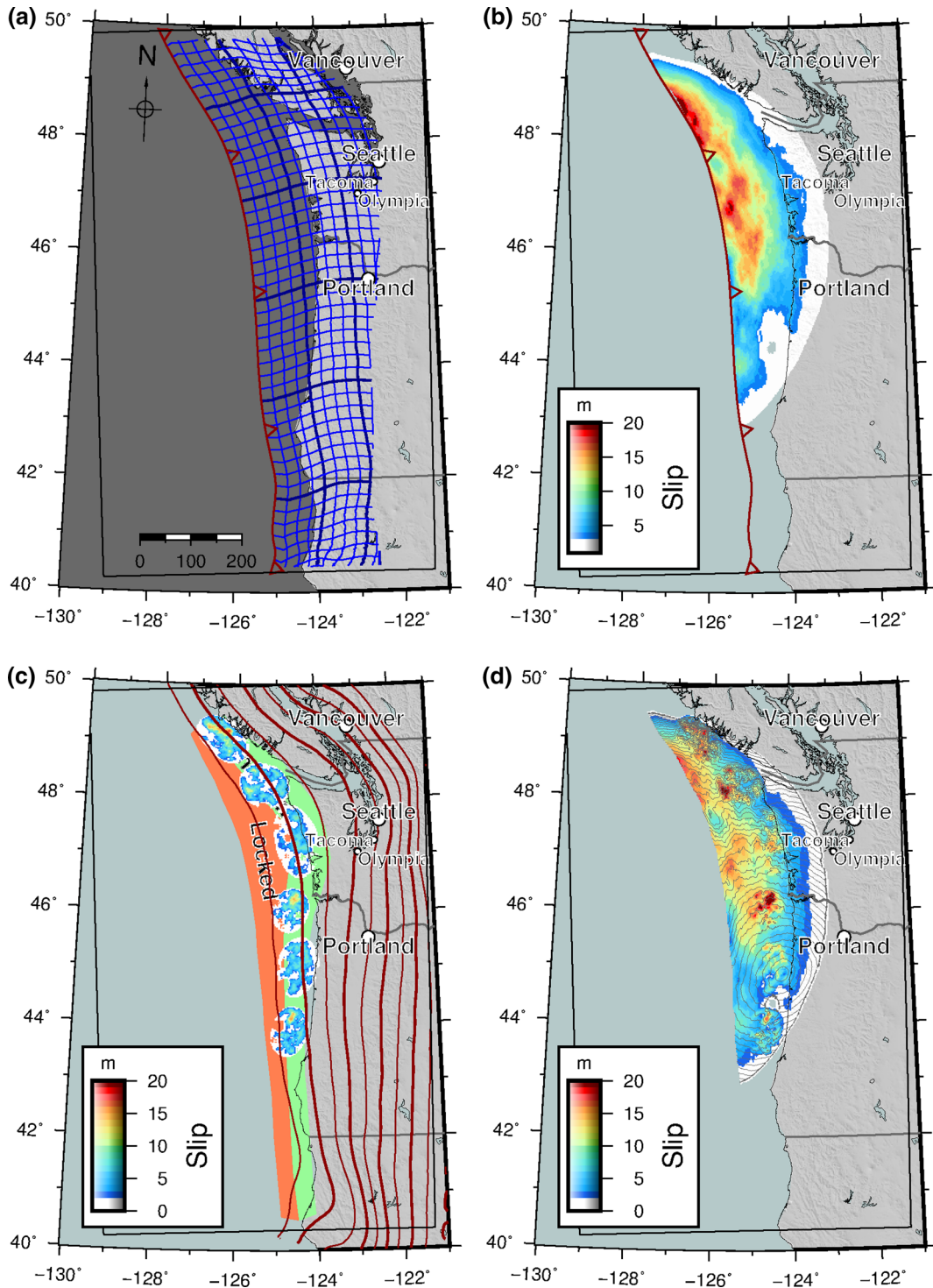
on the 3-D representation of the subducting slab surface (Blair et al. 2011). First, along-strike and along-dip distances were computed on iso-depth contours of the slab surface, with strike distances tracked along the contour and dip distances computed in the direction perpendicular to the contours. Next

the corresponding strike and dip position of each subfault was established from the contour values (Fig. 3a) by linear interpolation. The strike and dip positions on the curved slab were then used to interpolate rupture parameters defined on a planar fault for each subfault in the finite difference grid. Figure 3b shows the background slip on the irregular fault obtained from rupture model D.

The slip distribution of the subevents was also generated using a von Karman autocorrelation function, but with shorter autocorrelation lengths of 50 km (Mai and Beroza 2002). The subevents cover a circular area of about 100 km diameter each, with the subevent magnitude ranging from 7.9 to 8.1. The five subevents were placed at along-dip distances between 60 and 120 km, which puts them at depths of $\sim$ 20 km near the center of the transition zone (Fig. 3c), shallower than the 30–40 km depth identified for subevents or strong motion generation areas in studies of the Tohoku earthquake (Frankel 2013; Kurahashi and Irikura 2013). To analyze the impact of subevent depth on ground motions, we also performed one simulation with the subevents moved further to the east, at depths between 25 and 30 km (rupture model A'). The total slip of each rupture scenario (Fig. 3d) was obtained by superimposing the five subevents on the background slip model (i.e., the total slip on a subfault is the sum of the background slip and the subevent slip), resulting in a total event magnitude between 9 and 9.1.

Following Frankel (2017), we computed rupture initialization times for each subfault using the distance from the subfault to the hypocenter, x_i, and the secant rupture velocity associated with that subfault, v_{ri},

$$t_i = {x_i}/{v_{ri}} + \sigma_i,$$

with the random value σ_i chosen from a uniform distribution between $\pm$ 0.4 s. The secant rupture velocity v_{ri} is derived from an assumed average rupture velocity $\bar{v}_r$ and a perturbation reflecting the difference between total local slip u_i and average slip $\bar{u}$ (Frankel 2017):

$$v_{ri} = \bar{v}_r + c(u_i - \bar{u}).$$

The constant c is determined by specifying a standard deviation of 10%, and the average rupture

velocity is set to 2500 m/s (Frankel 2017). This definition results in slightly higher rupture velocities in areas of higher slip, which is consistent with findings from dynamic rupture simulations (Guatteri et al. 2003).

The rise time of each subfault was obtained by dividing the total slip by the slip velocity. We adopted background and subevent slip velocities of 1.3 m/s and 5.4 m/s, respectively, from Frankel (2017), which produces a shorter rise time and higher dynamic stress drop for the subevents than for the background slip. In the case of the Tohoku earthquake, this choice resulted in good agreement between simulated and observed spectra (Frankel 2017).

The strike and dip angle on each subfault was computed directly from the irregular slab geometry. To compute the slip azimuth, we used the direction of motion of the JdF plate with respect to the North American (NA) plate along the JdF plate boundary from the Global Strain Rate Model (GSRM v 2.1) (Kreemer et al. 2014). This results in a slip direction between 35 and 55° along the JdF-NA plate boundary as a result of the clockwise rotation of the JdF plate (Wilson 1993). Rake was computed by taking the difference between the local slip azimuth and strike direction, and adding a random component using a normal distribution with a standard deviation of 45°. We generated a suite of different slip realizations to investigate the variability of ground motions with source parameters.

4. Wave Propagation Simulation

We simulated the wave propagation from the suite of source models using the AWP-ODC code, which uses an explicit finite difference formulation on a staggered grid that is fourth-order accurate in space and second-order accurate in time. AWP was originally developed by Olsen (1994) for single-CPU computers and later optimized for multiple-CPU systems using MPI (Cui et al. 2010). A modern, highly scalable version of AWP supporting GPU accelerators was introduced in 2013 (Cui et al. 2013) for kinematic sources. The latest release of the CPU and GPU versions of AWP support frequency-

dependent viscoelastic attenuation (Withers et al. 2015) and Drucker-Prager plasticity (Roten et al. 2016).

The accuracy of AWP was verified against two independent finite difference and finite element codes by Bielak et al. (2010) in the framework of the ShakeOut earthquake preparedness exercise (Jones et al. 2008). Goodness-of-fit metrics between synthetic ground motions derived from three different wave propagation codes showed that the three numerical methods produces consistent solutions. Simulations of the 2014 M 5.1 La Habra earthquake for frequencies up to 5 Hz also revealed very good agreement between the three codes (Bielak et al. 2016). Withers et al. (2015) verified the accuracy of AWP in modeling frequency-dependent Q (quality factor) against frequency-wavenumber solutions for a layered halfspace model. Withers et al. (2015) also validated AWP against strong-motion data recorded during the 2008 M_w 5.4 Chino Hills earthquake for frequencies up to 5 Hz and the 1994 M_w 6.7 Northridge earthquake for frequencies up to 7.5 Hz (Withers et al. 2018).

Because the original implementation of AWP employs a spatially uniform (equidistant) grid over the entire computational domain, the higher-velocity material making up most of the computational domain is significantly overdiscretized in a typical scenario simulation. Nie et al. (2017) developed a method for seismic wavefield estimation using a discontinuous mesh interface (WEDMI) for the 3D fourth-order staggered-grid FD scheme used by AWP. The discontinuous mesh (DM) method operates by exchanging wavefield information between media partitions discretized with two different grid spacings, which alleviates the problem of overdiscretization and improves efficiency. Recently WEDMI was implemented in the scalable GPU version of AWP, and the method was verified against uniform mesh solutions by simulating the M 5.1 La Habra earthquake (Roten et al. 2018).

The discontinuous mesh version of AWP (AWP-GPU-DM) was also used for the simulations presented here. We first verified the accuracy of the DM solution for the Cascadia scenarios by performing both a uniform and DM mesh solution for the same scenario (rupture model A). For the uniform mesh solution, a grid spacing of 100 m was used throughout the computational domain, resulting in a mesh size of $6540 \times 10{,}730 \times 600$ grid points. For the discontinuous mesh solution, the small grid interval of 100 m was only used in the uppermost 8 km, and a larger interval of 300 m was used for the rest of the domain; the resulting grid sizes were $6540 \times 10{,}728 \times 80$ grid points for the fine and $2180 \times 3576 \times 176$ grid points for the coarse mesh. The uniform mesh solution required ~ 3.4 h using 4440 Kepler K20X GPUs on the OLCF Titan supercomputer, while the discontinuous mesh solution required 480 GPUs for ~ 7.3 h. Use of the DM reduced the computational cost by a factor of 4.3 for a model depth of 60 km, while the savings are significantly larger if a model depth of 120 km is used.

Although DM methods sometimes suffer from numerical instabilities especially in the presence of strong velocity contrasts inside the mesh overlap zone (Kristek et al. 2010; Nie et al. 2017), the Cascadia simulations remained stable for the entire duration of the computation (90,000 time steps), which produced 450 s of synthetic ground motions. The stability of WEDMI was recently improved with the introduction of wavefield smoothing in the vertical direction (Roten et al. 2018), which resulted in stable results during simulations of the M 5.1 La Habra earthquake including small-scale heterogeneities.

Peak ground velocities (PGVs) for rupture model A obtained with the discontinuous mesh FD method are very similar to those obtained from the uniform solution (Fig. 4). Because the sponge zones in the coarse grid contain less grid points than those in the fine or uniform grids, minor differences are expected close to the domain boundaries. Time series extracted at sites of interest also exhibit no notable difference between the two methods (Fig. 5).

5. Ground Motion Simulation Results

We simulated ground motions for four different realizations of background slip distributions (A, B, C and D). For the slip distribution in rupture model A, we also varied the location of subevents, the depth extent of the model and the response of near-surface sediments (linear vs. nonlinear) to analyze the sensitivity of ground
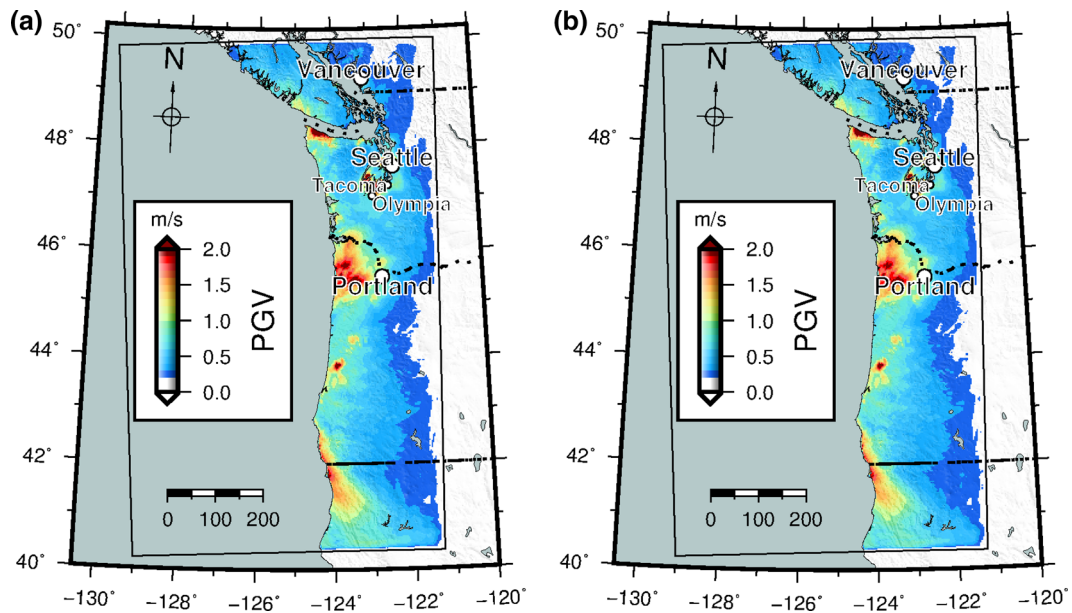
Figure 4
Peak ground velocities (PGVs) from rupture scenario A' obtained with **a** uniform mesh and **b** discontinuous mesh method in AWP
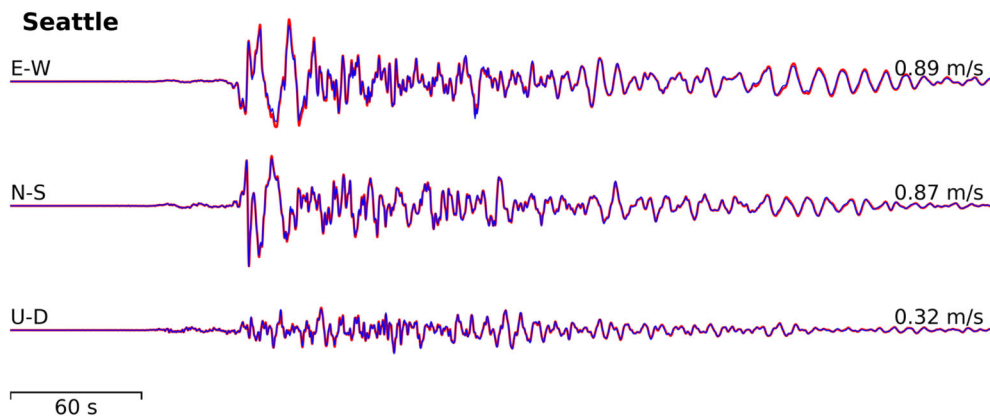

Figure 5
Synthetic seismograms in downtown Seattle obtained from rupture model A' using uniform (thick red lines) and discontinuous (thin blue lines) mesh solutions. Numbers above traces indicate peak velocity

motions to these parameters (Fig. 6). Slip distribution D was used in two different hypocenter locations to study effects of rupture propagation direction.

5.1. Influence of Model Depth

Ground motions obtained from slip distribution A with the shallow model (60 km maximum depth) reach 0.73 m/s in the Seattle and 0.25 m/s in the Vancouver downtown areas (Fig. 8a and Table 1). If

the model depth is increased to 120 km (rupture model A +), PGVs increase to 0.83 and 0.35 m/s in Seattle and Vancouver, respectively (Fig. 8b and Table 1). The depth of the model also increases simulated spectral accelerations (SAs) in Vancouver, but does not affect PGVs or SAs in Portland (Table 1). This might suggest that ground motions are enhanced by the impedance contrast between the continental crust and the subducted slab beneath the Vancouver and Seattle regions, where the depth of
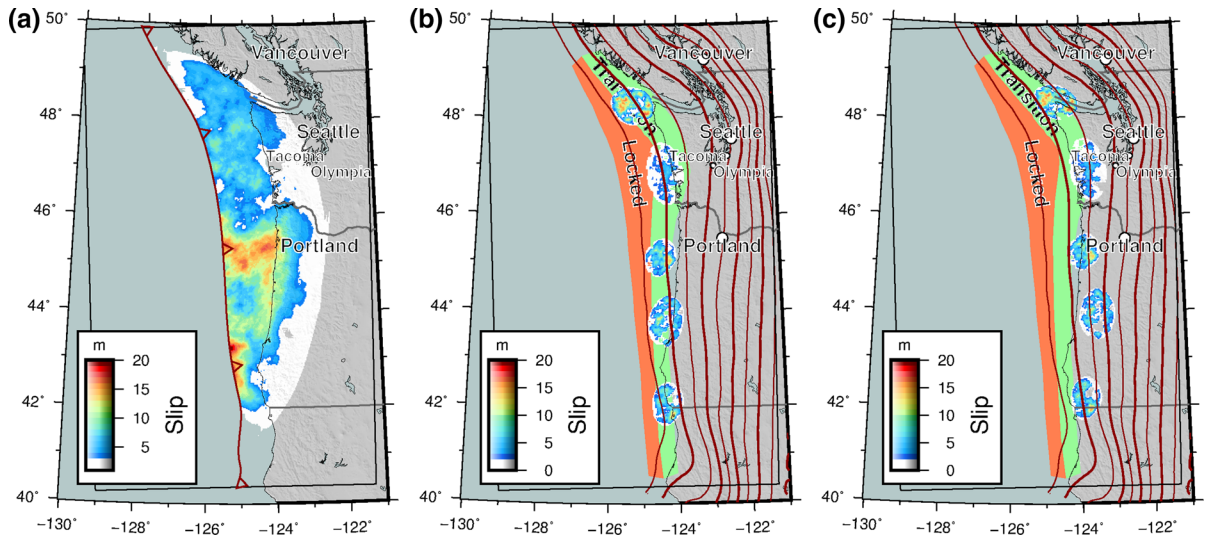
Figure 6

a Background slip in rupture models A and A', **b** subevents in rupture model A, and **c** subevents in rupture model A' (moved further to the east)

Table 1

Simulated ground motions in Seattle, Vancouver and Portland from different slip realizations and model variations

Site	Seattle				Vancouver				Portland			
Scenario	PGV (m/s)	SA (m/s^2)			PGV (m/s)	SA (m/s^2)			PGV (m/s)	SA (m/s^2)		
		5 s	2 s	1.5 s		5 s	2 s	1.5 s		5 s	2 s	1.5 s
A	0.73	0.97	1.85	2.73	0.25	0.48	1.04	1.76	0.43	0.37	2.03	4.39
A+	0.83	0.97	1.87	2.66	0.35	0.49	1.21	1.81	0.45	0.37	2.01	4.53
A++	0.85	0.99	1.83	2.62	0.35	0.50	1.13	1.79	0.45	0.37	2.00	4.62
A'	1.00	2.09	3.57	3.81	0.31	0.49	1.02	1.62	0.96	0.81	5.37	9.39
Ap	0.72	0.92	1.86	2.56	0.25	0.46	1.00	1.65	0.43	0.35	2.01	4.33
B	0.79	1.77	2.86	3.44	0.34	0.69	1.15	1.26	0.47	0.63	1.75	4.22
C	0.60	1.28	1.75	2.55	0.32	0.47	1.33	1.21	0.24	0.29	1.35	1.79
Dn	0.57	1.52	2.56	3.22	0.24	0.28	1.23	2.73	0.59	0.55	2.29	3.82
Ds	0.86	1.76	3.10	3.42	0.54	0.77	1.35	1.56	0.29	0.31	1.62	3.06

A+, A++: Slip distribution A using maximum domain depths of 120 km and 240 km, respectively

A': Slip distribution A with subevents moved $\sim$ 75 km to the east

Ap: Slip distribution B simulated with Drucker-Prager plasticity in near-surface sediments

Dn, Ds: Slip distribution D rupturing from north to south and south to north, respectively (120 km domain depth)

the upper slab boundary exceeds the depth extent of the shallow model. This interpretation is supported by Fig. 7a, which shows the ratio between PGVs obtained using the 120 and 60 km model. PGV ratios above 1.25 are only encountered in the eastern part of the domain, where the slab depth is larger than

50 km. We note that, although the shallow domain extends to 60 km depth, the absorbing boundaries at the bottom of the model limit the effective depth to 51 km (we used a thickness of 30 grid points for the sponge zones with a grid spacing of 300 m). On the other hand, increasing the domain size to 240 km
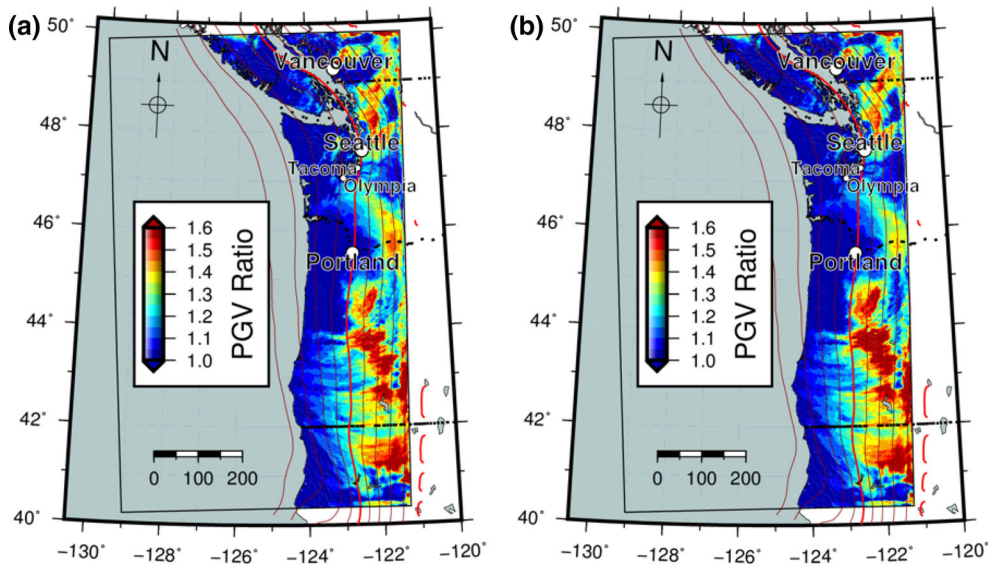
Figure 7
Ratio between PGVs obtained using **a** 120 km deep (scenario A +) and 60 km deep simulation (scenario A) and **b** 240 km deep (scenario A ++) and 60 km deep (scenario A) simulation. Brown contours show slab depth in 10 km intervals, the red line shows the 50 km depth contour
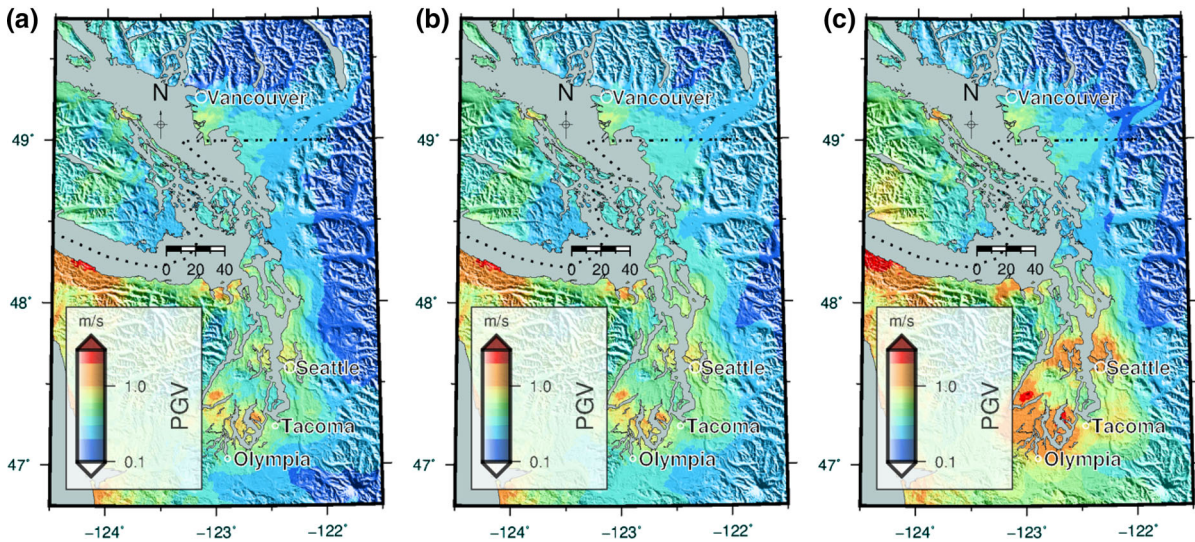

Figure 8
PGVs in the Seattle and Vancouver areas from **a** rupture model A with 60 km domain depth, **b** A + with 120 km domain depth and **c** A' with subevents moved ∼ 75 km to the east

(model A ++) does not lead to significantly different ground motion prediction (Fig. 7b, Table 1) compared to using 120 km (model A).

5.2. Sensitivity of Ground Motions to Subevent Location

Because seismic waves in the frequency band relevant for buildings are emitted mostly by the

subevents, the location of subevents is an important factor controlling the ground motions.

Figure 8c shows peak ground velocities in the Seattle and Vancouver areas obtained in rupture model A', which uses the same background and subevent slip distributions as model A, but with the subevents moved ∼ 75 km to the east. Because this shift puts the urban centers of Seattle, Tacoma and Olympia closer to the second northernmost subevent (Fig. 6c), it results in larger ground motions in these areas (Fig. 8c), with PGVs above 1 m/s obtained in downtown Seattle (Table 1). Although we consider the subevent locations to be more realistic in rupture model A (e.g., rupture contained mostly in the transition and locked zones) than in model A', the sensitivity of ground motions to the subevent location is important, and it underlines the need to better understand and predict the depth-varying rupture properties of subduction zone earthquakes.

5.3. Plastic Yielding in Sedimentary Basins

Although nonlinear effects are usually considered to be important only at high frequencies ($f > 1$ Hz), some studies suggest that they may also affect long-period surface waves (Joyner 2000; Roten et al. 2014). To assess if this nonlinearity would affect long-period ground motions in Cascadia during a megathrust event, we simulated the ground motion from slip distribution A (60 km model depth) inside a medium governed by Drucker-Prager plasticity (referred to as simulation Ap in Table 1). We only considered nonlinear effects in the shallow crust where the shear-wave velocity v_s is smaller than 2000 m/s. We assumed a friction angle of 30° and a cohesion of zero for mesh points with shear-wave velocities below 750 m/s. For nodes with 750 m/s $\leq v_s \leq$ 2000 m/s, we used the Hoek–Brown failure criterion (Hoek 1994) to predict the yield stress for a moderately fractured sandstone at the given depth. We then computed equivalent friction angles and cohesions pertaining to the Hoek–Brown failure stress, which were used to evaluate the Drucker-
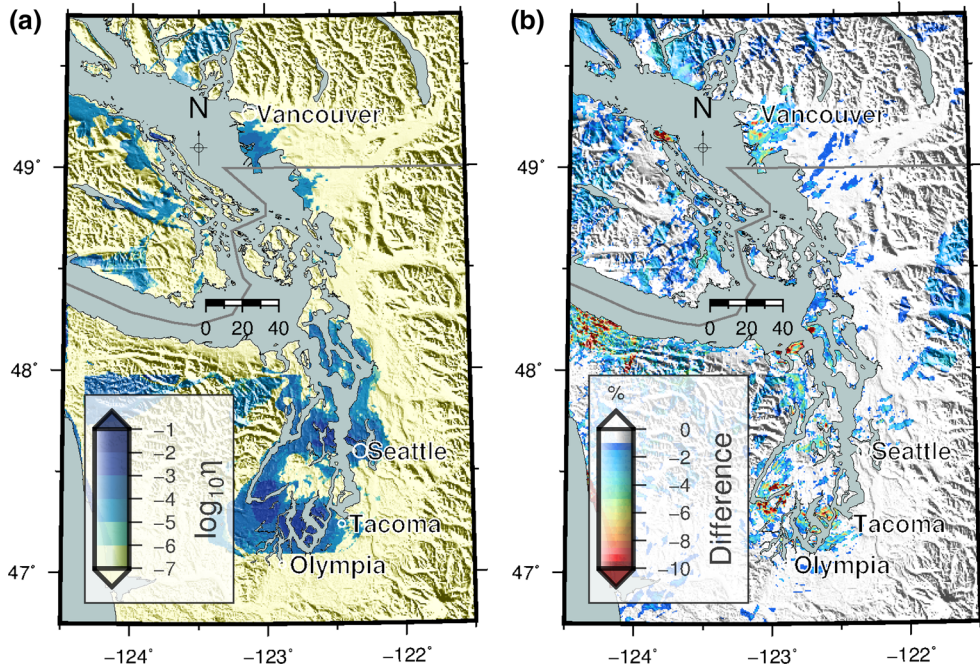

Figure 9
Simulation of scenario Ap (rupture model A with Drucker-Prager plasticity). **a** Permanent plastic strain and **b** difference in PGV (%) with respect to linear scenario A in Vancouver-Seattle areas
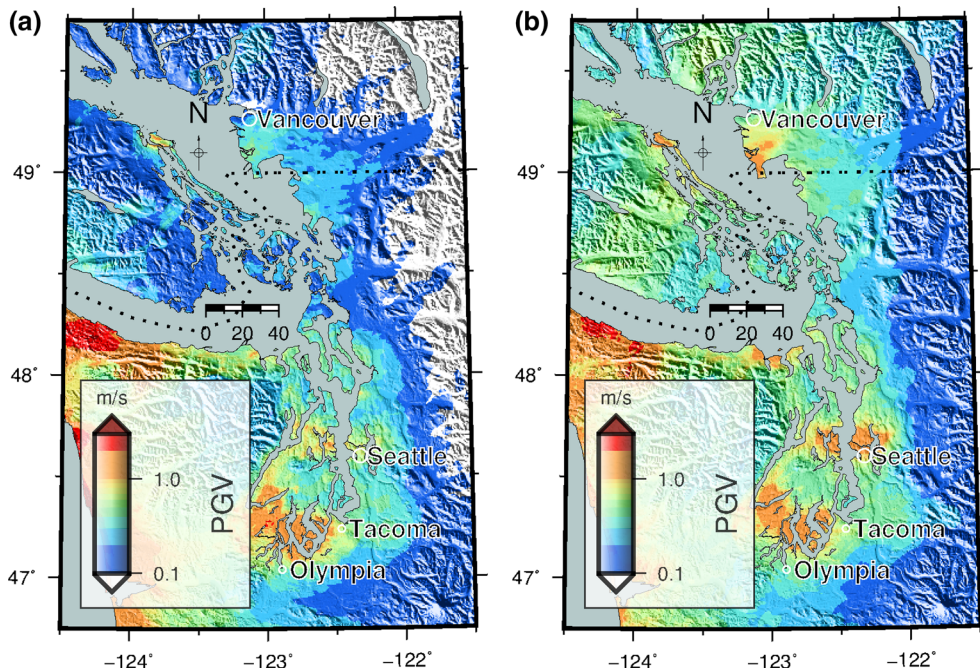
Figure 10
PGVs from **a** scenario Dn rupturing from north to south, and **b** scenario Ds rupturing from south to north

Prager yield condition in AWP (Roten et al. 2017). For simplicity we assumed isotropic stress conditions and a water table located at the surface.

Figure 9a shows the principal plastic strain at the surface obtained from the nonlinear scenario Ap. Large deformations occur in the deep sediments of the Seattle basin and the Fraser river delta south of Vancouver. However, the plastic behavior of these sediments does not significantly affect ground motions at the frequencies considered here ($f \leq 1.25$ Hz), and the difference between the linear scenario A and the nonlinear scenario Ap only exceeds 10% in isolated areas (Fig. 9b) and is almost negligible for the sites considered in Table 1. We cannot exclude that the absence of nonlinear effects is a consequence of enforcing a minimum shear-wave velocity of 625 m/s throughout the medium. The importance of plastic effects should be reassessed using higher-resolution 3D simulations, which would be able to include Holocene sediments with $v_s < 625$ m/s, which are encountered especially in the south Greater Vancouver area (Molnar 2011; Molnar et al. 2014), and in the Seattle basin (Williams et al. 1999).

5.4. Effect of Rupture Propagation Direction

Finally, we investigate how the rupture propagation direction would affect ground motions in the Seattle and Vancouver regions. Figure 10 compares PGVs obtained from rupture scenario Dn, propagating from north to south, with scenario Ds, propagating from south to north. The direction of rupture propagation completely changes the distribution of PGVs especially in the northern half of the map. In rupture scenario Ds, PGVs exceed 1 m/s south of Vancouver and in the Seattle area, but they remain below 1 m/s in scenario Dn.

The pattern of 2 s-SAs, on the other hand, exhibits less sensitivity to the direction of rupture propagation (Fig. 11), and 2 s-SAs above 2 m/s^2 are predicted south of Vancouver and in the Seattle region for both scenario Dn and Ds. This observation indicates that effects of rupture propagation direction are frequency-dependent, as expected from source directivity effects.

Simulated seismograms in Vancouver are dominated by long-period ($T \approx 10$ s) phases arriving after approximately 150 s in scenario Ds (Fig. 12), but not
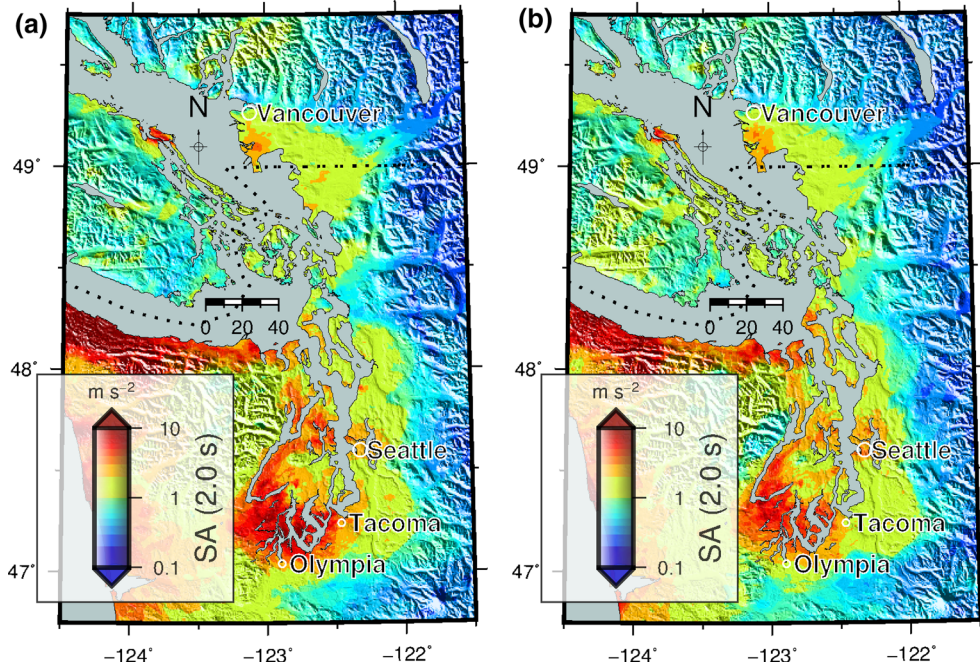
Figure 11
2 s-SAs from model D rupturing **a** from north to south (Dn) and **b** from south to north (Ds)

in scenario Dn. These long-period wavetrains, emitted from the background slip and enhanced by effects of source directivity, control the large PGVs obtained in scenario Ds, while the PGVs are controlled by shorter-period arrivals from the subevents in scenario Dn. Maximum Fourier amplitude spectra of the simulated velocity in Vancouver and Seattle (Fig. 13) occur at ∼ 0.08 Hz for both scenario Dn and Ds, but with a much higher peak amplitude in

scenario Ds than in scenario Dn. At frequencies above approximately 0.4 Hz, the spectra become insensitive to the rupture propagation direction.

This frequency-dependency suggests that effects of source directivity are important at long periods (> 10 s), where constructive interference enhances the amplitude of long wavelengths emitted by the background slip in the direction of rupture propagation. However, the lack of a clear directivity effect at
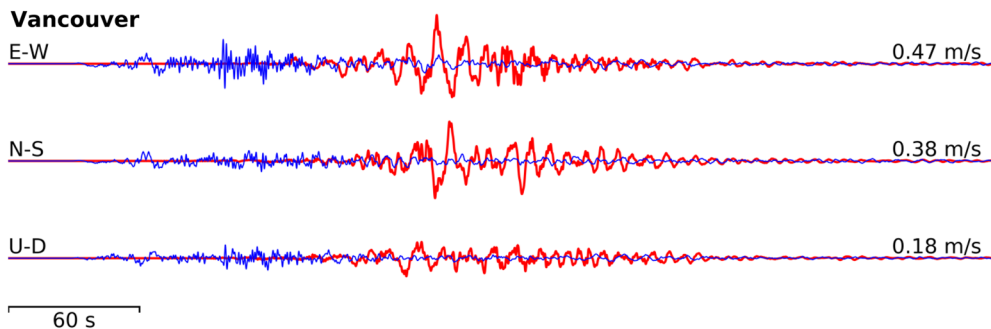

Figure 12
Simulated ground motion in downtown Vancouver for scenario Dn rupturing from north to south (thin blue lines) and scenario Ds rupturing from south to north (thick red lines)
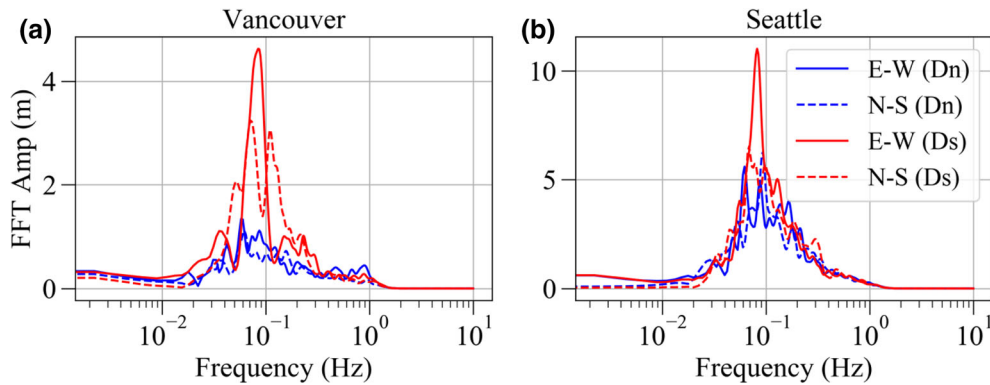
Figure 13
Fourier amplitude of simulated velocities in **a** Vancouver and **b** Seattle from scenarios Dn (rupture from north to south) and Ds (rupture from south to north)

higher frequencies indicates that the short-period wavefronts emitted from the subevents are not coherent enough to give rise to constructive interference. This frequency-dependence of source directivity was also reported by Wirth et al. (2018), who noted strong directivity effects at periods above 1 s.

PGVs predicted in Seattle range between 0.57 and 1 m/s, which is higher than the value of 0.42 m/s reported by Olsen et al. (2008). However, Olsen et al. (2008) only simulated one scenario, which ruptured unilaterally towards the south from a northern hypocenter located offshore Vancouver Island. Not surprisingly, the PGV values predicted by Olsen et al. (2008) are closest to those we obtained for scenario Dn (0.57 m/s PGV in Seattle), which also nucleates in the north. In addition, these early simulations were limited to frequencies below 0.5 Hz, and the source was specified from slip inversion results which did not include the high-frequency subevents of the Sumatra–Andaman earthquake (Lay et al. 2012), which contribute significantly to the ground motions.

6. Summary

We have carried out wave propagation simulations for a suite of M9 megathrust scenarios in the Cascadia subduction zone. An integrated and expanded velocity model of the region was generated by incorporating a local, higher-resolution model of the

Georgia basin (Molnar et al. 2014) into the larger Cascadia CVM (Stephenson et al. 2017), and extending the model to greater depth. We have generated an ensemble of kinematic source models, each composed of a background slip distribution with long rise time and superimposed subevents with short rise time to mimic the frequency-varying rupture properties observed in past subduction zone earthquakes (Lay et al. 2012). In addition to simulating four different realizations of background and subevent slip distributions, we considered variations within these rupture models to study the sensitivity of ground motions to subevent location, computational domain depth, plastic yielding in near-surface sediments and rupture directivity effects.

Simulations were carried out using the discontinuous mesh version of the AWP finite difference code, which was verified against a uniform mesh solution for one of our rupture scenarios. Peak ground velocities range between 0.72 and 1.00 m/s in downtown Seattle and between 0.25 and 0.54 m/s in downtown Vancouver, where spectral accelerations at 2 s range between 1.75 and 3.75 m/s^2 and 1.04 and 1.35 m/s^2, respectively.

In the northeastern corner of the computational domain including Vancouver, where the depth of the subducting slab exceeds 60 km, higher PGVs are obtained if the computational domain is extended to 120 km, compared to a simulation performed with a mesh of 60 km depth defined in the Pacific Northwest CVM V1.6. Ground motions in Seattle are sensitive

to the location of subevents, which control the shaking in the frequency range relevant for buildings ($f > 0.1$ Hz). Effects of Drucker-Prager plasticity are not important at frequencies below 1.25 Hz if shear-wave velocities are clipped at 625 m/s, even though the yield stress of near-surface sediments is exceeded in the Seattle basin and in southern Vancouver.

Effects of rupture directivity are important at the long periods emitted by the background slip distribution, and long-period wavetrains emitted in the direction of rupture propagation may lead to large PGVs in the Seattle and Vancouver areas. This rupture direction effect was not observed at frequencies above ~ 0.4 Hz. Future simulations should consider different variations in the rupture time of the subevents to corroborate this frequency-dependence of rupture directivity effects.

FD simulations currently in preparation will further reduce the grid spacing and use additional grid resolutions for increased efficiency. The minimum shear-wave velocity within the basins will be lowered and a geotechnical layer will be added to the CVM to better approximate near-surface conditions.

Publisher's Note Springer Nature remains neutral with regard to jurisdictional claims in published maps and institutional affiliations.

REFERENCES

Bielak, J., R. Taborda, K. Olsen, R. Graves, F. Silva, N. Khoshnevis, W. Savran, D. Roten, Z. Shi & C. Goulet (2016). Verification and validation of high-frequency (f_{max} = 5 Hz) ground motion simulations of the 2014 M 5.1 La Habra, California, earthquake. AGU Fall Meeting Abstracts.

Bielak, J., Graves, R. W., Olsen, K. B., Taborda, R., Ramírez-Guzmán, L., Day, S. M., et al. (2010). The ShakeOut earthquake scenario: Verification of three simulation sets. *Geophysical Journal International, 180*(1), 375–404.

Blair, J. L., McCrory, P., Oppenheimer, D., & Waldhauser, F. (2011). *A geo-referenced 3D model of the Juan de Fuca slab and associated seismicity*. Washington: US Geological Survey.

Brocher, T. M. (2005). Empirical relations between elastic wavespeeds and density in the Earth's crust. *Bulletin of the Seismological Society of America, 95*(6), 2081–2092.

Cassidy, J. F. & G. C. Rogers (2004). Variation in ground shaking on the Fraser River delta (Greater Vancouver, Canada) from analysis of moderate earthquakes. Proceedings of the 13th World Conference on Earthquake Engineering.

Chai, C., Ammon, C. J., Maceira, M., & Herrmann, R. B. (2015). Inverting interpolated receiver functions with surface wave dispersion and gravity: application to the western US and adjacent Canada and Mexico. *Geophysical Research Letters, 42*(11), 4359–4366.

Cui, Y., K. B. Olsen, T. H. Jordan, K. Lee, J. Zhou, P. Small, D. Roten, G. Ely, D. K. Panda and A. Chourasia (2010). Scalable earthquake simulation on petascale supercomputers. High Performance Computing, Networking, Storage and Analysis (SC), 2010 International Conference for, IEEE.

Cui, Y., E. Poyraz, K. B. Olsen, J. Zhou, K. Withers, S. Callaghan, J. Larkin, C. Guest, D. Choi and A. Chourasia (2013). Physics-based seismic hazard analysis on petascale heterogeneous supercomputers. Proceedings of the International Conference on High Performance Computing, Networking, Storage and Analysis, ACM.

Dash, R., Spence, G., Riedel, M., Hyndman, R., & Brocher, T. (2007). Upper-crustal structure beneath the Strait of Georgia, southwest British Columbia. *Geophysical Journal International, 170*(2), 800–812.

Delouis, B., J. M. Nocquet and M. Vallée (2010). Slip distribution of the February 27, 2010 Mw = 8.8 Maule earthquake, central Chile, from static and high-rate GPS, InSAR, and broadband

teleseismic data. Geophysical Research Letters 37(17), L1730, 1–7.

Frankel, A. (2013). Rupture history of the 2011 M 9 Tohoku Japan earthquake determined from strong-motion and high-rate GPS recordings: Subevents radiating energy in different frequency bands. *Bulletin of the Seismological Society of America, 103*(2B), 1290–1306.

Frankel, A. (2017). Modeling strong-motion recordings of the 2010 M w 8.8 Maule, Chile, earthquake with high stress-drop subevents and background slip. *Bulletin of the Seismological Society of America, 107*(1), 372–386.

Frankel, A., Stephenson, W., & Carver, D. (2009). Sedimentary basin effects in Seattle, Washington: Ground-motion observations and 3D simulations. *Bulletin of the Seismological Society of America, 99*(3), 1579–1611.

Frankel, A., Wirth, E., Marafi, N., Vidale, J., & Stephenson, W. (2018). Broadband synthetic seismograms for magnitude 9 earthquakes on the cascadia megathrust based on 3D simulations and stochastic synthetics, Part 1: Methodology and overall results. *Bulletin of the Seismological Society of America, 108*(5A), 2347–2369.

Galvez, P., Dalguer, L. A., Ampuero, J. P., & Giardini, D. (2016). Rupture reactivation during the 2011 M w 9.0 Tohoku earthquake: Dynamic rupture and ground-motion simulations. *Bulletin of the Seismological Society of America, 106*(3), 819–831.

Goldfinger, C., Galer, S., Beeson, J., Hamilton, T., Black, B., Romsos, C., et al. (2017). The importance of site selection, sediment supply, and hydrodynamics: A case study of submarine paleoseismology on the Northern Cascadia margin, Washington USA. *Marine Geology, 384,* 4–46.

Guatteri, M., Mai, P. M., Beroza, G. C., & Boatwright, J. (2003). Strong ground-motion prediction from stochastic-dynamic source models. *Bulletin of the Seismological Society of America, 93*(1), 301–313.

Han, S.-C., Shum, C., Bevis, M., Ji, C., & Kuo, C.-Y. (2006). Crustal dilatation observed by GRACE after the 2004 Sumatra-Andaman earthquake. *Science, 313*(5787), 658–662.

Hayashi, Y., Tsushima, H., Hirata, K., Kimura, K., & Maeda, K. (2011). Tsunami source area of the 2011 off the Pacific coast of Tohoku Earthquake determined from tsunami arrival times at offshore observation stations. *Earth Planets and Space, 63*(7), 54.

Heaton, T. H., & Hartzell, S. H. (1986). Source characteristics of hypothetical subduction earthquakes in the northwestern United States. *Bulletin of the Seismological Society of America, 76*(3), 675–708.

Hoek, E. (1994). Strength of rock and rock masses. *ISRM News Journal, 2*(2), 4–16.

Hyndman, R., & Wang, K. (1995). The rupture zone of Cascadia great earthquakes from current deformation and the thermal regime. *Journal of Geophysical Research: Solid Earth, 100*(B11), 22133–22154.

IRIS. (2015). Data Services Products: EMC-WUS-CAMH-2015 3D shear-wave velocity model of the western United States. from https://ds.iris.edu/ds/products/emc-wus-camh-2015/. Accessed 2 Jan 2019.

Jones, L. M., Bernknopf, R., Cox, D., Goltz, J., Hudnut, K., Mileti, D., et al. (2008). The shakeout scenario. *US Geological Survey Open-File Report, 1150,* 308.

Joyner, W. B. (2000). Strong motion from surface waves in deep sedimentary basins. *Bulletin of the Seismological Society of America, 90*(6B), S95–S112.

Koper, K. D., Hutko, A. R., Lay, T., Ammon, C. J., & Kanamori, H. (2011). Frequency-dependent rupture process of the 2011 M w 9.0 Tohoku Earthquake: Comparison of short-period P wave backprojection images and broadband seismic rupture models. *Earth Planets and Space, 63*(7), 16.

Kreemer, C., Blewitt, G., & Klein, E. C. (2014). A geodetic plate motion and global strain rate model. *Geochemistry Geophysics Geosystems, 15*(10), 3849–3889.

Kristek, J., Moczo, P., & Galis, M. (2010). Stable discontinuous staggered grid in the finite-difference modelling of seismic motion. *Geophysical Journal International, 183*(3), 1401–1407.

Kurahashi, S., & Irikura, K. (2011). Source model for generating strong ground motions during the 2011 off the Pacific coast of Tohoku Earthquake. *Earth Planets and Space, 63*(7), 11.

Kurahashi, S., & Irikura, K. (2013). Short-period source model of the 2011 M w 9.0 Off the Pacific Coast of Tohoku earthquake. *Bulletin of the Seismological Society of America, 103*(2B), 1373–1393.

Lay, T., H. Kanamori, C. J. Ammon, K. D. Koper, A. R. Hutko, L. Ye, H. Yue and T. M. Rushing (2012). Depth-varying rupture properties of subduction zone megathrust faults. Journal of Geophysical Research: Solid Earth 117(B4), B04311, 1–21.

Ludwin, R. S., Dennis, R., Carver, D., McMillan, A. D., Losey, R., Clague, J., et al. (2005). Dating the 1700 Cascadia earthquake: Great coastal earthquakes in native stories. *Seismological Research Letters, 76*(2), 140–148.

Mai, P. M. and G. C. Beroza (2002). A spatial random field model to characterize complexity in earthquake slip. Journal of Geophysical Research: Solid Earth 107(B11), ESE 10, 1–21.

McCrory, P. A., J. L. Blair, F. Waldhauser and D. H. Oppenheimer (2012). Juan de Fuca slab geometry and its relation to Wadati-Benioff zone seismicity. Journal of Geophysical Research: Solid Earth 117(B9), B09306, 1–23.

Molnar, S. (2011). Predicting earthquake ground shaking due to 1D soil layering and 3D basin structure in SW British Columbia, Ph.D. Thesis, University of Victoria, 2011, Canada, 160 pages.

Molnar, S., Cassidy, J. F., Olsen, K. B., Dosso, S. E., & He, J. (2014). Earthquake ground motion and 3D Georgia basin amplification in southwest British Columbia: Deep Juan de Fuca plate scenario earthquakes. *Bulletin of the Seismological Society of America, 104*(1), 301–320.

Nie, S., Wang, Y., Olsen, K. B., & Day, S. M. (2017). Fourth-order staggered-grid finite-difference seismic wavefield estimation using a discontinuous mesh interface (WEDMI). *Bulletin of the Seismological Society of America, 107*(5), 2183–2193.

Olsen, K. B. (1994). Simulation of three-dimensional wave propagation in the Salt Lake Basin, Department of Geology and Geophysics, University of Utah

Olsen, K. B., Stephenson, W. J., & Geisselmeyer, A. (2008). 3D crustal structure and long-period ground motions from a M9.0 megathrust earthquake in the Pacific Northwest region. *Journal of Seismology, 12*(2), 145–159.

Roten, D., H. Miyake and K. Koketsu (2012). A Rayleigh wave back-projection method applied to the 2011 Tohoku earthquake. Geophysical Research Letters 39(2), L02302, 1–6.

Roten, D., Y. Cui, K. B. Olsen, S. M. Day, K. Withers, W. H. Savran, P. Wang and D. Mu (2016). High-frequency nonlinear earthquake simulations on petascale heterogeneous

supercomputers. Proceedings of the International Conference for High Performance Computing, Networking, Storage and Analysis, IEEE Press.

Roten, D., K. B. Olsen, S. Nie and S. M. Day (2018). High-frequency nonlinear earthquake simulations on discontinuous finite difference grid. 11th National Conference on Earthquake Engineering. Los Angeles, CA, Earthquake Engineering Research Institute.

Roten, D., Olsen, K., Day, S., & Cui, Y. (2017). Quantification of fault-zone plasticity effects with spontaneous rupture simulations. *Pure and Applied Geophysics, 174*(9), 3369–3391.

Roten, D., Olsen, K., Day, S., Cui, Y., & Fäh, D. (2014). Expected seismic shaking in Los Angeles reduced by San Andreas fault zone plasticity. *Geophysical Research Letters, 41*(8), 2769–2777.

Roten, D., Olsen, K., Pechmann, J., Cruz-Atienza, V., & Magistrale, H. (2011). 3D simulations of M 7 earthquakes on the Wasatch fault, Utah, Part I: Long-period (0–1 Hz) ground motion. *Bulletin of the Seismological Society of America, 101*(5), 2045–2063.

Stephenson, W. J. (2007). *Velocity and density models incorporating the Cascadia Subduction Zone for 3D earthquake ground motion simulations*. Washington: Geological Survey US.

Stephenson, W. J., N. G. Reitman and S. J. Angster (2017). P-and S-wave Velocity Models Incorporating the Cascadia Subduction Zone for 3D Earthquake Ground Motion Simulations—Update for Open-File Report 2007–1348, US Geological Survey.

Suzuki, W., Aoi, S., Sekiguchi, H., & Kunugi, T. (2011). Rupture process of the 2011 Tohoku-Oki mega-thrust earthquake (M9.0) inverted from strong-motion data. *Geophysical Research Letters, 38*, L00G16.

UNAVCO. (2018). Plate motion calculator. From https://www.unavco.org/software/geodetic-utilities/plate-motion-calculator/plate-motion-calculator.html. Accessed 2 Jan 2019.

USGS. (2011). A geo-referenced 3D model of the Juan de Fuca Slab and Associated seismicity. From https://pubs.usgs.gov/ds/633/. Accessed 2 Jan 2019.

Wang, D. & J. Mori (2011a). Frequency-dependent energy radiation and fault coupling for the 2010 Mw8. 8 Maule, Chile, and 2011 Mw9. 0 Tohoku, Japan, earthquakes. Geophysical Research Letters 38(22), 2460–2473.

Wang, D., & Mori, J. (2011b). Rupture process of the 2011 off the Pacific coast of Tohoku Earthquake (Mw 9.0) as imaged with back-projection of teleseismic P-waves. *Earth Planets Space, 63*, 603–607.

Wang, P. L., Engelhart, S. E., Wang, K., Hawkes, A. D., Horton, B. P., Nelson, A. R., et al. (2013). Heterogeneous rupture in the great Cascadia earthquake of 1700 inferred from coastal subsidence estimates. *Journal of Geophysical Research: Solid Earth, 118*(5), 2460–2473.

Williams, R. A., Stephenson, W. J., Frankel, A. D., & Odum, J. K. (1999). Surface seismic measurements of near-surface P-and S-wave seismic velocities at earthquake recording stations, Seattle, Washington. *Earthquake Spectra, 15*(3), 565–584.

Wilson, D. S. (1993). Confidence intervals for motion and deformation of the Juan de Fuca plate. *Journal of Geophysical Research: Solid Earth, 98*(B9), 16053–16071.

Wirth, E. A., Frankel, A. D., Marafi, N., Vidale, J. E., & Stephenson, W. J. (2018). Broadband synthetic seismograms for magnitude 9 earthquakes on the Cascadia megathrust based on 3D simulations and stochastic synthetics, Part 2: Rupture parameters and variability. *Bulletin of the Seismological Society of America, 108*(5A), 2370–2388.

Wirth, E. A., Frankel, A. D., & Vidale, J. E. (2017). Evaluating a Kinematic Method for Generating Broadband Ground Motions for Great Subduction Zone Earthquakes: Application to the 2003 Mw 8.3 Tokachi-Oki EarthquakeEvaluating a Kinematic Method for Generating Broadband Ground Motions. *Bulletin of the Seismological Society of America, 107*(4), 1737–1753.

Withers, K. B., K. B. Olsen, Z. Shi and S. M. Day (2018). Validation of deterministic broadband ground motion and variability from dynamic rupture simulations of buried thrust earthquakes. Bulletin of the Seismological Society of America. https://doi.org/10.1785/0120180006.

Withers, K. B., Olsen, K. B., & Day, S. M. (2015). Memory-efficient simulation of frequency-dependent Q. *Bulletin of the Seismological Society of America, 105*(6), 3129–3142.

Witter, R. C., Y. Zhang, K. Wang, C. Goldfinger, G. R. Priest and J. C. Allan (2012). Coseismic slip on the southern Cascadia megathrust implied by tsunami deposits in an Oregon lake and earthquake-triggered marine turbidites. Journal of Geophysical Research: Solid Earth **117**(B10), B10303, 1–17.